Are extreme dissipation events predictable in turbulent fluid flows?

Patrick J. Blonigan, Mohammad Farazmand, and Themistoklis P. Sapsis

Phys. Rev. Fluids **4**, 044606 — Published 17 April 2019

DOI: 10.1103/PhysRevFluids.4.044606

Are extreme dissipation events predictable in turbulent fluid flows?

Patrick J. Blonigan
NASA Ames Research Center, Moffett Field, CA 94035, United States

Mohammad Farazmand* and Themistoklis P. Sapsis†
Department of Mechanical Engineering, Massachusetts Institute of Technology, Cambridge, MA 02139, United States

We derive precursors of extreme dissipation events in a turbulent channel flow. Using a recently developed method that combines dynamics and statistics for the underlying attractor, we extract a characteristic state that precedes laminarization events that subsequently lead to extreme dissipation episodes. Our approach utilizes coarse statistical information for the turbulent attractor, in the form of second order statistics, to identify high-likelihood regions in the state space. We then search within this high probability manifold for the state that leads to the most finite-time growth of the flow kinetic energy. This state has both high probability of occurrence and leads to extreme values of dissipation. We use the alignment between a given turbulent state and this critical state as a precursor for extreme events and demonstrate its favorable properties for prediction of extreme dissipation events. Finally, we analyze the physical relevance of the derived precursor and show its robust character for different Reynolds numbers. Overall, we find that our choice of precursor works well at the Reynolds number it is computed at and at higher Reynolds number flows with similar extreme events.

I. INTRODUCTION

Turbulent fluid flows have been the most challenging paradigm of chaotic behavior with signatures of persistent and intermittent (i.e. over finite-times and at arbitrary time instants) instabilities leading to nonlinear energy transfers between scales. These nonlinear energy transfers are responsible for both the broad band character of the spectrum but also for the non-Gaussian statistics. More specifically, while non-zero third order statistics are primarily responsible for the persistent non-linear energy transfers (turbulent cascades) and the shape of the spectrum [38, 39], intermittent events, such as dissipation bursts, are primarily responsible for the heavy tail characteristics [17, 32, 33].

Here we are interested in the formulation of precursors for predicting these extreme events. These are important in problems related to atmospheric and climate science, fluid-structure interactions, and turbulent fluid flow control, just to mention a few. We present our analysis on a standard configuration of a turbulent fluid flow, namely the channel flow, that exhibits extreme events in the form of large dissipation episodes occurring in random times [28]. These extreme events rise out of a high-dimensional turbulent attractor essentially without any clear warning. They have the form of a short-time excursion towards laminarization of the flow and a subsequent burst of turbulent kinetic energy which leads to a large dissipation episode pushing the flow away from the laminar state.

Many aspects of these intermittent bursts remain elusive primarily because of the intrinsic high dimensionality of the underlying turbulent attractor that limits the applicability of existing mathematical approaches [15, 18]. In particular, extreme events due to their rare character cannot

* mfaraz@mit.edu
† Corresponding author: sapsis@mit.edu, Tel: (617) 324-7508, Fax: (617) 253-8689

be 'seen' effectively by energy-based methods, such as Proper Orthogonal Decomposition (POD). Even if one tries to consider conditional POD modes during extreme events these will not necessarily give the modes related to the triggering of the extreme events, as these do not necessarily obtain high energy, even during the extreme event.

A different class of methods focus on the spectral analysis of the underlying Koopman operator [31, 36], and strive to extract unstable modes associated with certain observables of the system. Such unstable modes are typically estimated by Dynamic Mode Decomposition (DMD) [6, 40, 43]. This analysis, however, can only detect modes associated with long-term instabilities which do not seem to explain short-term intermittent events observed in turbulent flows [2, 16]. Other variants, however, such as multi-resolution DMD [29] have been demonstrated to work well in systems with relatively low-dimensional attractors.

Extreme events in complex dynamical systems have also been analyzed recently using Large Deviation Theory (LDT), e.g. in nonlinear water waves [10]. The basic idea is to search the phase space for initial conditions associated with a given magnitude of the objective function (observable of interest) and then from those pick the one with the highest probability of occurrence. However, these efforts have shown to work well in systems where the core of the attractor has Gaussian statistics. For different cases there is no rigorous foundation for LDT to operate. Even in the Gaussian case, the resulting optimization problem has very high dimensionality to be practically solvable for an application like the one considered here – see [37] for a detailed discussion.

Here we apply a recently developed framework for the discovery of precursors to extreme events [17]. This framework formulates the precursors as solutions to a constrained optimization problem (note that a formally similar approach was presented in [35] to identify small perturbations of the laminar flow for transition to turbulence). In contrast to LDT, in the present approach we consider a set of high probability initial conditions, based on a rough approximation of the attractor, and then search within this set for the initial state that has the highest growth for the quantity of interest. An adjoint solver is employed to compute the gradient of the objective function. Because the search is constrained within a low-dimensional (but high-probability) set, the feasibility set, the resulted optimization problem is computationally tractable. The solution provides with an initial state that has high probability to occur and leads to rapid growth of the objective function (in our case the kinetic energy). We discuss the physical relevance of the derived critical state in the context of the turbulent channel flow and use the alignment with this critical state as a scalar precursor for the prediction of future extreme events. We measure the effectiveness of the precursor through direct numerical experiments and examine its robustness over different Reynolds numbers. The success of our approach to an intermittently turbulent channel paves the way for studying transitional flows, such as bypass transition of boundary layers.

This paper is organized as follows. In Section II we described the minimal channel flow used in this work and discuss various aspects of the problem. The optimization problem for discovering the precursor to extreme events is presented in Section III. In Section IV we present a statistical analysis quantifying the predictive power of the optimal precursor. Finally, our concluding remarks are presented in Section V.

II. TURBULENT CHANNEL FLOW - PHENOMENOLOGY

A. The minimal flow unit for channel flows

Turbulent channel flow has been a staple of numerical studies of turbulence for many years [28]. The chaotic nature of these simulations makes it difficult to analyze local spatiotemporal events and

physical mechanisms in them, such as the formation and destruction of individual hairpin vortices in the near-wall region. To isolate these physical mechanisms and others, work has been done to find "minimal flow units" for various regions of the channel. Jimenez and Moin [24] found the minimal flow unit for near wall turbulence for several low Reynolds number flows by considering turbulent channel flow simulations with domains that were considerably smaller than conventional channel flow simulations. These smaller domains eliminate larger scale turbulent structures but accurately resolved the near-wall turbulent flow, matching turbulent flow statistics from experiments and prior numerical studies up to 40 wall units in the wall-normal direction.

Various minimal flow units have been used in a range of different studies because of its isolation of a few physical mechanisms and its relatively low computational cost. Carlson and Lumley used the minimal flow unit to study flow control strategies for turbulent boundary layers [4]. Minimal flow units have also been used to study near-wall and log-layer turbulence [19, 25, 26]. These studies use forcing functions to achieve turbulent flows in half-channels, and to selectively damp larger scale flow structures. Recently, near-wall minimal flow units have been used to study and characterize the effects of wall-roughness on wall-bounded flows and to build models of wall roughness effects [7, 30]. The near-wall minimal flow unit has also been used to demonstrate shadowing-based adjoint sensitivity analysis [3].

In addition, the near-wall minimal flow unit simulations routinely show highly intermittent behavior which is of interest for the purposes of our study. In certain low Reynolds number simulations, the flow on one wall exhibits turbulent behavior while the other remains laminar. The flow on both walls transitions at seemingly random intervals: the laminar wall would become turbulent, and then the turbulent wall would become laminar. Turbulent flow in the near-wall minimal flow unit is itself intermittent when it occurs. Time series of wall shear stress show that turbulence undergoes a cycle where it proliferates rapidly or "bursts", then decays slowly. This observation led to numerous subsequent studies into the intermittent nature of near-wall turbulence using minimal flow units (see Refs [22, 23], for comprehensive reviews).

B. Flow Solver

In this study we consider near-wall minimal flow units similar to those considered in Ref. [24]. We use a Discontinuous-Galerkin spectral-element method (DGSEM) framework to simulate the minimal flow unit with the compressible Navier-Stokes equations [8]. The DGSEM framework has been successfully applied to a range of different flows including channels flows and the near-wall minimal flow unit [9, 12, 20]. Also, it has an adjoint capability [5] that has been validated for the near-wall minimal flow unit in Ref. [3]. A detailed description of the discretization and implementation of this solver is available in Refs. [11] and [13].

We run a direct numerical simulation (DNS) of the channel flow with the compressible Navier-Stokes equations with a constant forcing in the axial direction to drive the channel. Since the Mach number is low, the effective governing equations reduce to the incompressible Navier–Stokes equations

$$\boldsymbol{\nabla} \cdot \boldsymbol{u} = 0, \tag{1a}$$

$$\partial_t \boldsymbol{u} + \boldsymbol{u} \cdot \boldsymbol{\nabla} \boldsymbol{u} = \frac{f_0}{\rho} \boldsymbol{e}_1 - \frac{1}{\rho} \boldsymbol{\nabla} p + \nu \Delta \boldsymbol{u}, \tag{1b}$$

$$\boldsymbol{u}(\boldsymbol{x}, 0) = \boldsymbol{u}_0(\boldsymbol{x}) \tag{1c}$$

where $\boldsymbol{u} = (u, v, w)$ denotes the three-dimensional velocity field with streamwise component u, wall-normal component v and spanwise component w. The constant forcing in the streamwise direction is denoted by f_0 and $\boldsymbol{e}_1 = (1, 0, 0)$ is the unit vector in the streamwise direction. The boundary conditions are no-slip at the walls so that $\boldsymbol{u}(x, \pm\delta, z, t) = 0$, and periodic in the spanwise and streamwise directions. Here, the channel height in the wall-normal direction is 2δ.

C. Numerical experiment set-up

The case we consider has a domain size of $\pi\delta \times 2\delta \times 0.34\pi\delta$ in the streamwise, wall-normal, and spanwise directions, respectively. The channel half-height δ was set to 1.0. The flow considered is at Reynolds number $Re = 2200$ (corresponding to the friction Reynolds number $Re_\tau = 110$) unless stated otherwise. The Reynolds number Re is defined as $Re = \rho U \delta/\mu$ where ρ is the fluid density, U is the centerline velocity of a laminar flow with the same mass flow rate (as in Ref. [24]), and μ is the dynamic viscosity. As in Ref. [3], U was chosen so that the Mach number of the flow was under 0.3 and therefore the flow is nearly incompressible. Note that the Reynolds number corresponding to bulk velocity for this case is roughly 1500.

The friction Reynolds number Re_τ is defined as $Re_\tau = \rho u_\tau \delta/\mu$ where $u_\tau = \sqrt{\tau_w/\rho}$ is the friction velocity and τ_w is the average shear stress at the wall. The channel constant forcing f_0 is set to balance the mean shear stress of the walls, so it is set by the choice of Reynolds number Re, and the friction Reynolds number Re_τ as follows

$$f_0 = \frac{\tau_w}{\delta} = \frac{Re_\tau^2}{Re}\rho U \tag{2}$$

The domain is discretized with a $4 \times 16 \times 2$ mesh with 8th order spatial elements, resulting in a $32 \times 128 \times 16$ distribution of nodes (65536 total), similar to the mesh used in Ref. [24]. The choice of $Re_\tau = 110.0$ results in grid resolutions of $\Delta x^+ \approx 11$ and $\Delta z^+ \approx 7$ wall units per node, where $x^+ = u_\tau x/\nu$, $y^+ = u_\tau y/\nu$, and $z^+ = u_\tau z/\nu$.

The wall-normal spacing corresponds to $\Delta y^+ \approx 0.6$ for the nodes closest to the walls, which ensures that the simulations are well resolved. We used space-time elements that were 4th order in time and the time slab (temporal element) was $\Delta t = 0.05 t_e$, where $t_e = \delta/U$ denotes the eddy turnover time, the time scale associated with the largest possible eddy in the channel.

The DGSEM flow solver used here has been validated for the minimal flow unit at $Re = 3000$ (equivalent to bulk velocity Reynold number of 2000) [3] and we carried out a similar validation study for the $Re = 2200$ case. Note that the statistics at $Re = 2200$ were only computed over time intervals when both walls had turbulent flow, as was done in Ref. [24] for low Reynolds number cases. This was necessary because the $Re = 2200$ flow exhibited intermittent behavior similar to that observed in previous studies of minimal flow units.

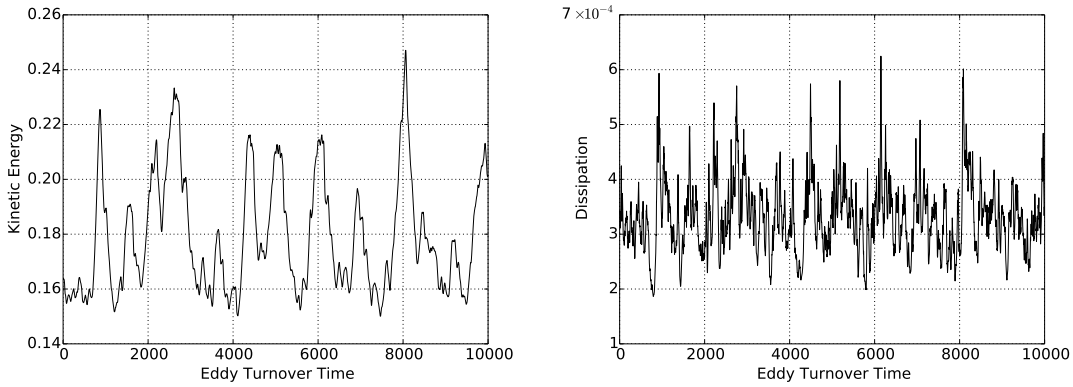

(a) (b)

FIG. 1: Time evolution of the kinetic energy (a) and the energy dissipation rate (b) for the near-wall minimal flow unit at $Re = 2200$

D. Extreme events

The intermittent behavior of the flow at $Re = 2200$ can be seen in Fig. 1 from the spikes in kinetic energy $E(t)$ and dissipation $Z(t)$. We define the kinetic energy,

$$E(t) = \iiint_{\Omega} \rho \boldsymbol{u} \cdot \boldsymbol{u} \, \mathrm{d}x \, \mathrm{d}y \, \mathrm{d}z, \tag{3}$$

where Ω is the flow domain. Note that this is the total kinetic energy, comprised of both the mean and turbulent kinetic energy of the flow. Energy dissipation rate $Z(t)$ is defined as

$$Z(t) = \iiint_{\Omega} \mathrm{tr}(\boldsymbol{\tau} \nabla \boldsymbol{u}) \, \mathrm{d}x \, \mathrm{d}y \, \mathrm{d}z, \tag{4}$$

where $\boldsymbol{\tau}$ denotes the stress tensor, defined as $\boldsymbol{\tau} = \mu(\nabla \boldsymbol{u} + \nabla \boldsymbol{u}^{\top})$ for an incompressible flow.

Fig. 1 shows that large increases in $E(t)$ are followed by spikes in $Z(t)$ and a subsequent decrease in $E(t)$. These large spikes in kinetic energy occur when there is laminar flow near one wall, and nearly laminar flow near the other wall. Laminar flows correspond to higher kinetic energy $E(t)$ because the channel is driven by a constant body force in the axial direction. This body force acts as a fixed axial pressure gradient. The body force and wall shear stress balance one another when the flow is in an equilibrium state where we have

$$\mu \frac{\partial \overline{u}}{\partial n} = \delta \frac{\partial \overline{p}}{\partial x}, \tag{5}$$

where n is the wall-normal direction. For a given centerline velocity, a laminar flow will exert less shear stress $\mu \frac{\partial \overline{u}}{\partial n}$ on the walls than a turbulent flow, so for a given wall shear stress $\mu \frac{\partial \overline{u}}{\partial n}$ the laminar flow will have a larger centerline velocity than a turbulent flow.

Therefore, the large spikes in $E(t)$ are the result of a flow laminarization event. Of course, the flow never completely reaches the laminar state, though it gets very close it. Figs. 2 and 3 show an example of a typical laminarization event where the flow undergoes the following stages.

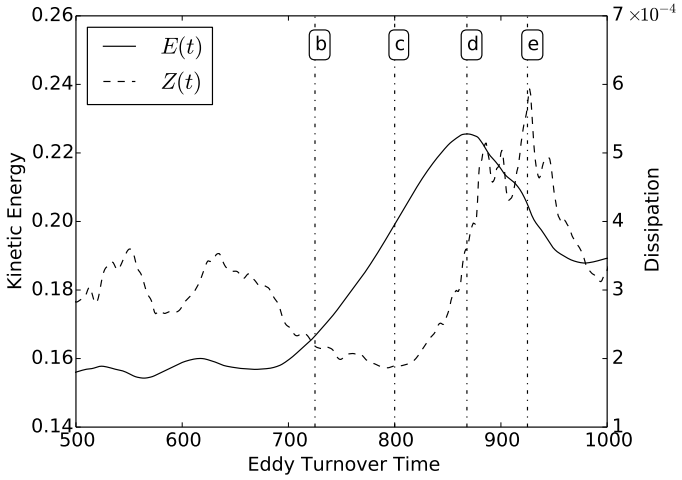

FIG. 2: Time evolution of $E(t)$ and $Z(t)$ during the first laminarization event shown in Fig. 1. The vertical lines indicate the times that snapshots in Fig. 3 correspond to. The first and last snapshot correspond to the start and end of the time horizon shown above.

1. The flow on the bottom wall becomes laminar (Fig. 3(b)).
2. The flow on the top wall becomes nearly laminar (Fig. 3(c)).
3. As the entire channel becomes nearly laminar, the axial velocity increases.
4. The higher velocities make the effective Reynolds number of the flow larger. This increases the likelihood of turbulent burst occuring since the flow is less stable to perturbations at a larger Reynolds number.
5. A turbulent burst occurs on the top wall, which causes $Z(t)$ to increase rapidly (Fig. 3(d)).
6. The bottom wall transitions to turbulence (Fig. 3(e)).
7. The turbulent flow on both walls causes $E(t)$ to decrease as it returns to the equilibrium mean turbulent flow profile (Fig. 3(f)).

These flow laminarization events, and the resulting bursts of energy dissipation rate, are the extreme events we will consider in this paper.

III. OPTIMAL STATES FOR EXTREME EVENTS

We now describe the constrained optimization problem whose solutions determine the most likely triggers of extreme events. The method is presented in detail in Ref. [17] and is reviewed here for completeness. We describe the optimization problem in the context of the channel flow, outline the numerical method for obtaining its solutions and present our numerical results.

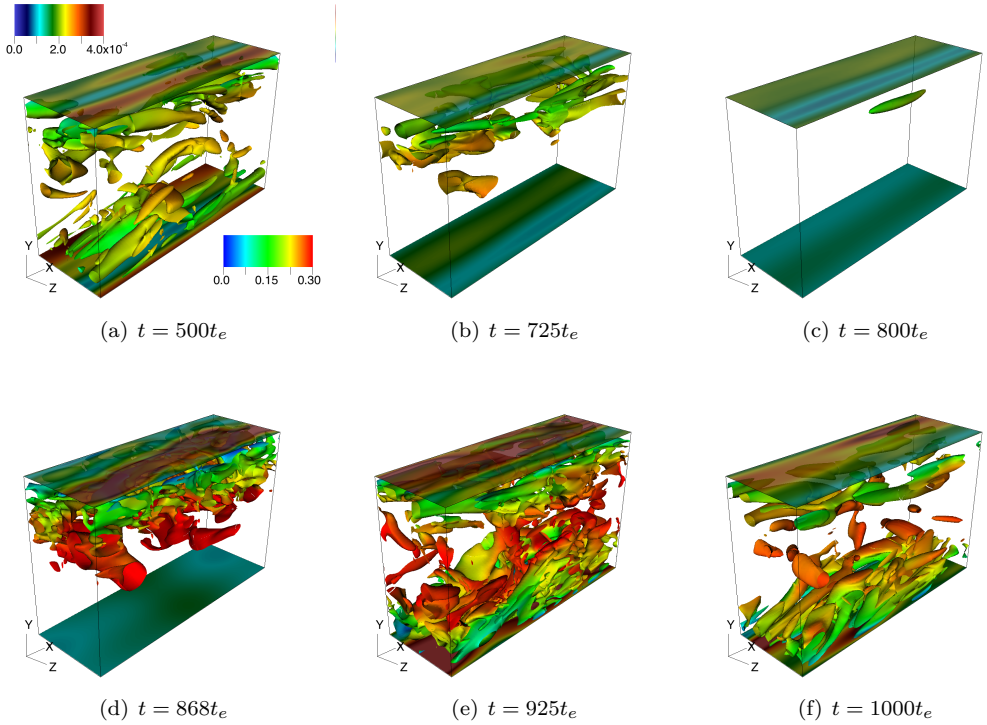

(a) $t = 500t_e$ (b) $t = 725t_e$ (c) $t = 800t_e$

(d) $t = 868t_e$ (e) $t = 925t_e$ (f) $t = 1000t_e$

FIG. 3: Snaphots of Q-criterion colored by axial velocity and wall shear stress. The axial velocity lies in the interval $[0, 0.3]$ and the wall shear stress lies in $[0, 4 \times 10^{-4}]$.

A. High-Likelihood triggers of extreme events

We seek initial states $\boldsymbol{u}_0$ that after a given integration time τ realize the largest possible energy growth. More precisely, we seek initial states $\boldsymbol{u}_0$ such that $E(\boldsymbol{u}(\tau)) - E(\boldsymbol{u}_0)$ is maximized. This is a PDE-constrained optimization problem, since the velocity field $\boldsymbol{u}(t)$ is required to satisfy the channel flow (1).

In addition to this PDE constraint, we also enforce a feasibility constraint, by requiring the initial state $\boldsymbol{u}_0$ to belong to the system attractor. This second constraint is essential in order to guarantee that the optimal solution is probabilistically relevant. As in many dissipative PDEs, the channel flow has an attractor towards which the solutions converge asymptotically after an initial transient. We are interested in the self-sustained and recurrent extreme events on this attractor as opposed to transient extreme events off the attractor that may occur but are not recurrent. In order to prevent the optimizer from considering such transient events, we enforce a feasibility constraint which is further elucidated in section III B.

With this prelude, the optimization problem can be formulated as

$$\max_{\boldsymbol{u}_0 \in \mathcal{U}} \big[E(\boldsymbol{u}(\tau)) - E(\boldsymbol{u}_0)\big], \tag{6a}$$

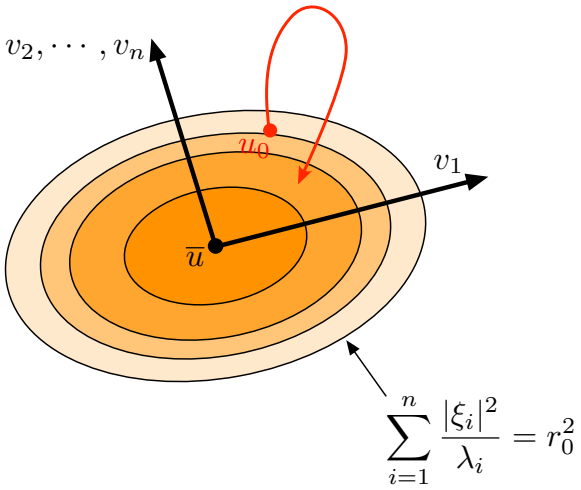

FIG. 4: A sketch of the proper orthogonal decomposition of the turbulent data. The attractor is approximated as an ellipsoid in the subspace spanned by the POD modes $\{\boldsymbol{v}_1, \cdots, \boldsymbol{v}_n\}$. The origin is the mean flow $\overline{\boldsymbol{u}}$.

$$\boldsymbol{u}(\tau) \text{ satisfies equation (1) with } \boldsymbol{u}(0) = \boldsymbol{u}_0, \tag{6b}$$

$$\boldsymbol{u}_0 \in \mathcal{A} \subset \mathcal{U}, \tag{6c}$$

where $\tau > 0$ is a prescribed time, related to the growth time scale of a typical extreme event. The constraint (6b) implies that $\boldsymbol{u}(\tau)$ is a solution of the channel flow. Constraint (6c) ensures that the optimizer belongs to the attractor $\mathcal{A}$ and is therefore probabilistically relevant. In the next section, we describe the method used to approximate the attractor $\mathcal{A}$.

B. Feasibility constraint and proper orthogonal decomposition

The attractors of dissipative dynamical systems are often very complex sets. Their estimation has been the subject of many studies (see e.g. [21]). Here, we approximate the attractors via Proper Orthogonal Decomposition (POD) of longterm simulations of the channel flow (this method is also known as the Principal Component Analysis). The POD approximation assumes that the attractor has a Gaussian distribution with mean $\overline{\boldsymbol{u}}(\boldsymbol{x})$ and covariance matrix $\boldsymbol{C}(\boldsymbol{x}, \boldsymbol{x}')$ where

$$\overline{\boldsymbol{u}}(\boldsymbol{x}) = \lim_{T\to\infty} \frac{1}{T} \int_0^T \boldsymbol{u}(\boldsymbol{x}, t) \mathrm{d}t, \tag{7a}$$

$$\boldsymbol{C}(\boldsymbol{x}, \boldsymbol{x}') = \lim_{T\to\infty} \frac{1}{T} \int_0^T (\boldsymbol{u}(\boldsymbol{x}, t) - \overline{\boldsymbol{u}}(\boldsymbol{x})) \otimes (\boldsymbol{u}(\boldsymbol{x}', t) - \overline{\boldsymbol{u}}(\boldsymbol{x}')) \, \mathrm{d}t. \tag{7b}$$

Let the vector fields $\boldsymbol{v}_i : \Omega \to \mathbb{R}^3$ denote the eigenfunctions of the covariance tensor, so that

$$\int_\Omega \boldsymbol{C}(\boldsymbol{x}, \boldsymbol{x}')\boldsymbol{v}_i(\boldsymbol{x}')\mathrm{d}\boldsymbol{x}' = \lambda_i \boldsymbol{v}_i(\boldsymbol{x}), \quad i \in \mathbb{N} \tag{8}$$

where $\lambda_i \in \mathbb{R}$ are the corresponding eigenvalues. The eigenvectors are ordered such that $\lambda_1 \geq \lambda_2 \geq \cdots$. Since the covariance tensor is symmetric and positive definite, the eigenvalues are real-valued and non-negative, and furthermore the eigenfunctions are orthogonal with respect to the L^2 inner product, i.e., $\langle \boldsymbol{v}_i, \boldsymbol{v}_j \rangle_{L^2(\Omega)} = \delta_{ij}$. We refer to the eigenfunctions $\boldsymbol{v}_i$ as the POD modes.

In the POD approximation, any state on the attractor is approximated as

$$\boldsymbol{u}(\boldsymbol{x}, t) = \overline{\boldsymbol{u}}(\boldsymbol{x}) + \sum_{i=1}^{n} \xi_i(t)\boldsymbol{v}_i(\boldsymbol{x}), \tag{9}$$

which is a finite-dimensional truncation to the first n POD modes. Each component of the vector $\boldsymbol{\xi} = (\xi_1, \cdots, \xi_n) \in \mathbb{R}^n$ is given by $\xi_i(t) = \langle \boldsymbol{u}(t) - \overline{\boldsymbol{u}}, \boldsymbol{v}_i \rangle_{L^2(\Omega)}$.

With this POD approximation of the attractor, the optimization problem (6) can be written more explicitly as

$$\max_{\boldsymbol{\xi} \in \mathbb{R}^n} \big[E(\boldsymbol{u}(\tau)) - E(\boldsymbol{u}_0)\big], \tag{10a}$$

$$\boldsymbol{u}(\boldsymbol{x}, \tau) \text{ satisfies equation (1) with } \boldsymbol{u}(\boldsymbol{x}, 0) = \boldsymbol{u}_0(\boldsymbol{x}), \tag{10b}$$

$$\boldsymbol{u}_0(\boldsymbol{x}) = \overline{\boldsymbol{u}}(\boldsymbol{x}) + \sum_{i=1}^{n} \xi_i \boldsymbol{v}_i(\boldsymbol{x}), \tag{10c}$$

$$\sum_{i=1}^{n} \frac{\xi_i^2}{\lambda_i} \leq r_0^2 \tag{10d}$$

where $r_0 \in \mathbb{R}$ is a prescribed parameter that is set equal to 1.0 in this study. Note that the form of the constraint essentially restricts our optimization within states that have the highest probability, given second-order statistics for the attractor. Constraint (10c) enforces that the mean-zero initial condition $\boldsymbol{u}_0 - \overline{\boldsymbol{u}}$ belongs to the subspace spanned by the first n POD modes. Constraint (10d), which describes an ellipsoid in the subspace $\mathrm{span}\{\boldsymbol{v}_1, \cdots, \boldsymbol{v}_n\}$, ensures that the initial conditions are not two far from the mean flow $\overline{\boldsymbol{u}}$ (see Fig. 4).

Although the initial condition $\boldsymbol{u}_0$ is constrained to the subspace spanned by the first n POD modes, the final state $\boldsymbol{u}(\tau)$ may not belong to this subspace. This is because the POD decomposition is only an approximation of the attractor, which represents initial states for our analysis, and not the exact invariant attractor. However, we take n large enough so that only an insignificant fraction of the energy content of the states on the attractor are neglected. More precisely, in the following, we set $n = 50$ so that the truncation of the turbulent states to these POD modes contain at least 90% of the kinetic energy, as shown in Fig. 5.

As discussed in section II D, previous studies of the minimal flow unit have shown that intermittent bursts of the flow originate from the near-wall activities. In light of these observations, we modify the

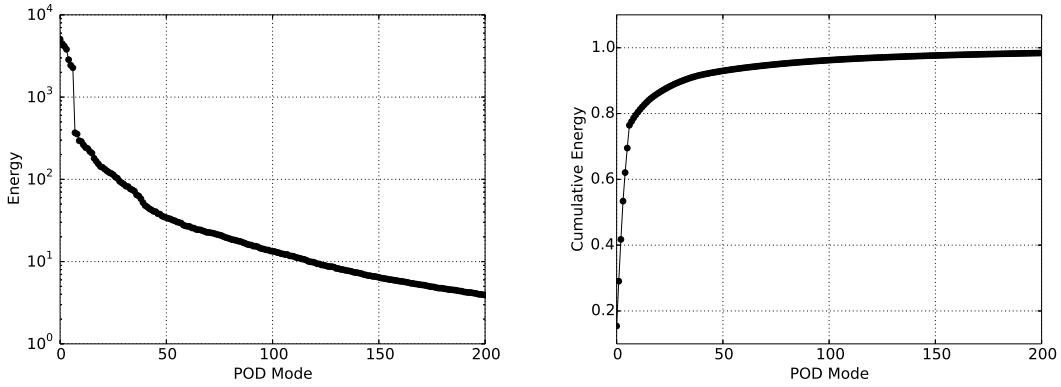

(a) (b)

FIG. 5: The energy content of the POD modes. (a) Energy content of each POD mode. (b) Cumulative energy content of the POD modes. POD was computed with 1000 snapshots at $Re = 2200$.

computation of the POD modes by multiplying the zero-mean velocity fields by a weight function that emphasizes the near-wall contribution of the flow. More precisely, we compute the weighted velocity fields

$$\boldsymbol{u}_{\epsilon,h}(\boldsymbol{x},t) = (\boldsymbol{u}(\boldsymbol{x},t) - \overline{\boldsymbol{u}}(\boldsymbol{x}))\, q_{\epsilon,h}(y), \tag{11}$$

by multiply the original velocity fields $\boldsymbol{u}$ (after removing the mean $\overline{\boldsymbol{u}}$) with the weight function

$$q_{\epsilon,h}(y) = \frac{1}{2}\left\{2 + \tanh\left[\frac{1}{\epsilon}\big(y - (\delta - h)\big)\right] - \tanh\left[\frac{1}{\epsilon}\big(y + (\delta - h)\big)\right]\right\}. \tag{12}$$

For $\epsilon \ll h \ll \delta$, the weight function $q_{\epsilon,h}$ vanishes near the center of the channel and approaches unity near the walls at $y = \pm\delta$ (see figure 6). The parameter h is the width of the near-wall region that we would like to emphasize and the small parameter ϵ determines how quickly the function $q_{\epsilon,h}$ decays to zero far from the walls.

We note that the weighting (11) is a linear operation on the velocity field, $\mathcal{L}(\boldsymbol{u}-\overline{\boldsymbol{u}}) := (\boldsymbol{u}-\overline{\boldsymbol{u}})q_{\epsilon,h}$, where the linear operator $\mathcal{L}$ is the multiplication by the weight $q_{\epsilon,h}$. It is straightforward to verify that $\mathcal{L}$ is a self-adjoint operator with respect to the $L^2(\Omega)$ inner product so that $\langle \mathcal{L}(\boldsymbol{u}_1-\overline{\boldsymbol{u}}), \mathcal{L}(\boldsymbol{u}_2-\overline{\boldsymbol{u}})\rangle_{L^2} = \langle (\boldsymbol{u}_1-\overline{\boldsymbol{u}}), \mathcal{L}^2(\boldsymbol{u}_2-\overline{\boldsymbol{u}})\rangle_{L^2}$ for all square integrable functions $\boldsymbol{u}_1, \boldsymbol{u}_2 \in L^2(\Omega)$. Therefore, introducing the weight function (11) is equivalent to replacing the L^2 inner product $\langle\cdot,\cdot\rangle_{L^2}$ withe 'weighted' inner product $\langle \cdot, \mathcal{L}^2\,\cdot\rangle_{L^2}$.

In practice, the POD modes are computed through the equations (7) and (8) except that in computing the covariance (7b) instead of the terms $\boldsymbol{u}(\boldsymbol{x},t) - \overline{\boldsymbol{u}}(\boldsymbol{x})$, we use the mean-zero weighted velocity $\boldsymbol{u}_{\epsilon,h}(\boldsymbol{x},t)$. In the following, we set $\epsilon = 0.1$ to keep the decay smooth. We selected $h = 25\delta/110$ to emphasize the near-wall flow up to ignore any flow above $y^+ \approx 50$, where the minimal flow unit does not capture all length scales. This modified POD not only emphasizes the near-wall contributions, but also speeds up the convergence of the numerical optimization of problem (10).

The POD modes were computed using 1000 snapshots taken from flows computed from 10 different randomly chosen, initial conditions. The snapshots were taken at intervals of 50 eddy turnover

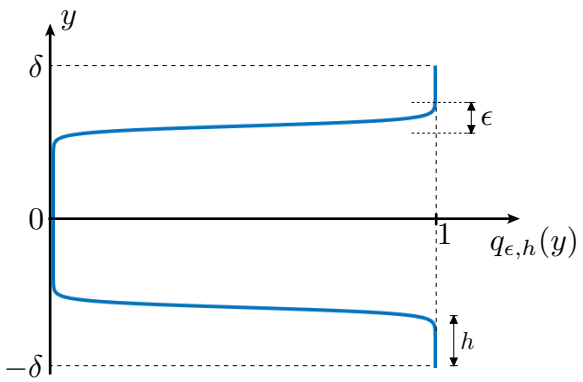

FIG. 6: A sketch of the weight function $q_{\epsilon,h}$ defined in (12).

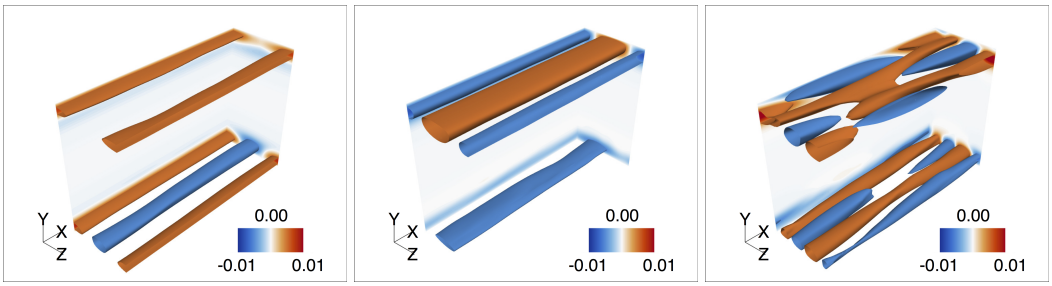

(a) Mode 1 (b) Mode 3 (c) Mode 11

FIG. 7: Contours and isosurfaces of axial velocity u for several POD modes. Isosurfaces are defined at $u = \pm 0.01$. Mode indicies are defined as in Fig. 5.

times to minimize any correlation in time. Fig. 5 shows the energy and cumulative energy of the POD modes. Almost 80% of the energy is captured by the first six modes, indicating that near-wall dynamics emphasized by our weight function are low dimensional.

Fig. 7 shows a few of these modes. The shape of the most energetic modes is dominated by long axial streaks which are know to be a main feature of the near-wall region [22]. The more energetic modes such as modes 1 and 3 contain wider streaks, while less energetic modes such as mode 11 contain thinner, less coherent streaks that meander slightly.

Finally, we point out that an energy-maximizing optimization similar to (6) was used in [35] in the context of subcritical transition to turbulence from the laminar state in the pipe flow. It is important to emphasize that the problem of extreme events discussed here is different from the subcritical transition to turbulence. Specifically, despite the formal similarities to the constrained optimization presented in [35], the optimal states relevant to extreme events are not lying in small neighborhoods around the laminar state. In fact, we do not utilize the existence of a laminar state, since we employ information for the full turbulent attractor, in contrast to [35] where all the analysis is formulated around the laminar state. The present study demands that the initial states belong to the turbulent attractor as enforced through the constraint (6c) and implemented numerically in this section. In particular, our constraint is a hyper-ellipsoid around the statistical mean $\overline{\boldsymbol{u}}$ (see equations

(10c)-(10d)). This set is not necessarily small and its extent is dictated by the flow dynamics (i.e., the eigenvalues λ_i of the covariance matrix).

Similarly, Farano et al. [14] investigated the observed bursts in a turbulent flow similar to our channel flow. However, they only require that the energy of the optimal state is prescribed, i.e., $E(\boldsymbol{u}_0) = E_0$ for a prescribed energy level E_0. This does not necessarily imply that the optimal state belongs to the attractor and therefore unphysical optimizers are not ruled out.

C. Numerical implementation

The optimization problem, equation (10), was solved using the Python package scipy [27]. Specifically, the "optimize" package was used and the optimization was carried out using Sequential Least SQuares Programming (SLSQP). The first constraint, (10b), is implicitly satisfied by the flow solver, which is called from Python using the "multiprocessing" module. The second and third constraints (10c)–(10d) and their gradients are implemented directly in Python. The convergence tolerance for the objective function was set to 10^{-7}. Otherwise the default convergence criterion were used. An adjoint solver was used to minimize the cost of computing the gradient of the objective function (10a). The DGSEM solver has a dual consistent, discrete adjoint formulation, details of which are discussed in Refs. [5, 8]. This adjoint solver allows us to compute the gradient at a computational cost similar to solving the primal, which is much cheaper than using finite differences to compute the gradient with respect to all $n = 50$ POD modes.

Since we use a gradient-based optimization, SLSQP seeks the local optimizers. Since the problem is highly non-convex, we are unaware of optimization methods that can provably guarantee the convergence to the global optimizer. Therefore, we run the SLSQP algorithm from several initial guesses $\boldsymbol{u}_0$ in the constraint set $\mathcal{A}$ and retain the local optimizer that corresponds to the largest energy growth among them.

D. Optimization results

The optimization was run from five different initial guesses $\boldsymbol{u}_0$ and with three different integration times of $\tau = 52.5t_e$, $\tau = 105t_e$, and $\tau = 210t_e$. The integration times correspond to roughly 1/8, 1/4, and 1/2 of the time scale of laminarization event similar to the one shown in Fig. 2. All five optimizations with $\tau = 52.5t_e$ and $\tau = 105t_e$ computed very similar optimal solutions $\boldsymbol{u}_0^*$. All these optimizers belong to the interior of the constraint set (10d), i.e. they satisfy $\sum_i \xi_i^2/\lambda_i < 1$. This does not imply that the constraint was not employed. On the contrary, the constraint was utilized during the optimization process to prevent the convergence to an optimal solution outside the constraint set. The optimization with an integration time of $\tau = 210t_e$ failed to converge because the adjoint grew very large in magnitude, and the gradient caused the optimizer to consider a non-physical solution in the ensuing line search.

Fig. 8 shows the convergence history of a typical optimization for $\tau = 52.5t_e$. The corresponding POD mode weights for the initial guess and optimal solution are shown in Fig. 9. The two largest POD modes in the optimal solution are modes 6 and 26, shown in Fig. 10. Together, these modes create the axial velocity deficit in the near wall region shown in Fig. 11. The maximum velocity deficit occurs roughly $y^+ = 18$ units from each wall, and decays to zero roughly $y^+ \approx 55$ units from the wall.

The region in which the velocity deficit occurs is known to have a major impact on near-wall turbulence. In [25] it was observed that damping axial velocity streaks or quasi-streamwise vortex

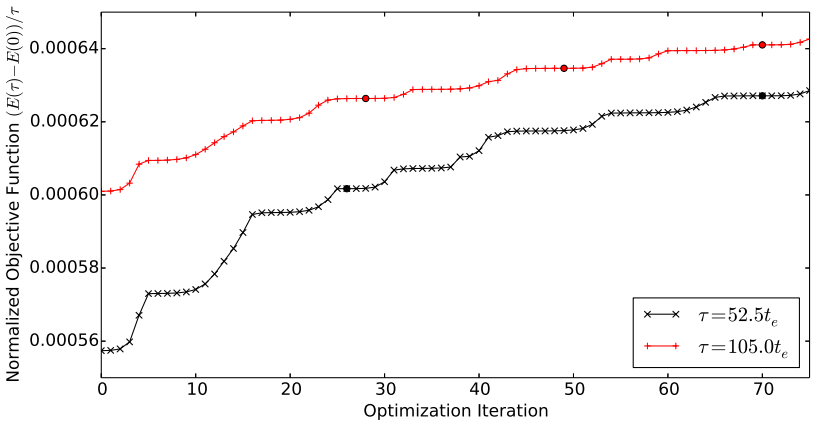

FIG. 8: Convergence of the objective function for the same initial guess but two different choices of τ. Solid dots represent instances when the optimizer was restarted.

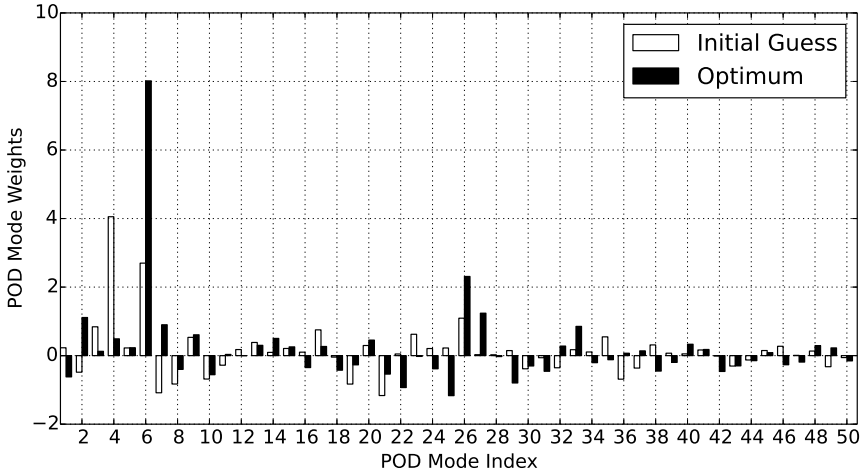

FIG. 9: POD mode weights for the initial guess and optimal solution.

structures between $y^+ \approx 20$ to $y^+ \approx 60$ led to laminarization of the near wall region. It appears that our optimal solution modifies the lower portion of this range. The relative uniformity of the axial velocity deficit results in the absence of axial velocity streaks and quasi-streamwise vortex structures. This is in contrast with the flow snapshots in Fig. 3, where the presence of low- and high-axial velocity streaks can be inferred from streaks in the wall shear stress, and quasi-axial structures are revealed by the q-criterion iso-contours. Without the axial velocity streaks and quasi-streamwise vorticity, the "streak-cycle" mechanism for the regeneration of near-wall turbulent fluctuations is broken and the flow laminarizes.

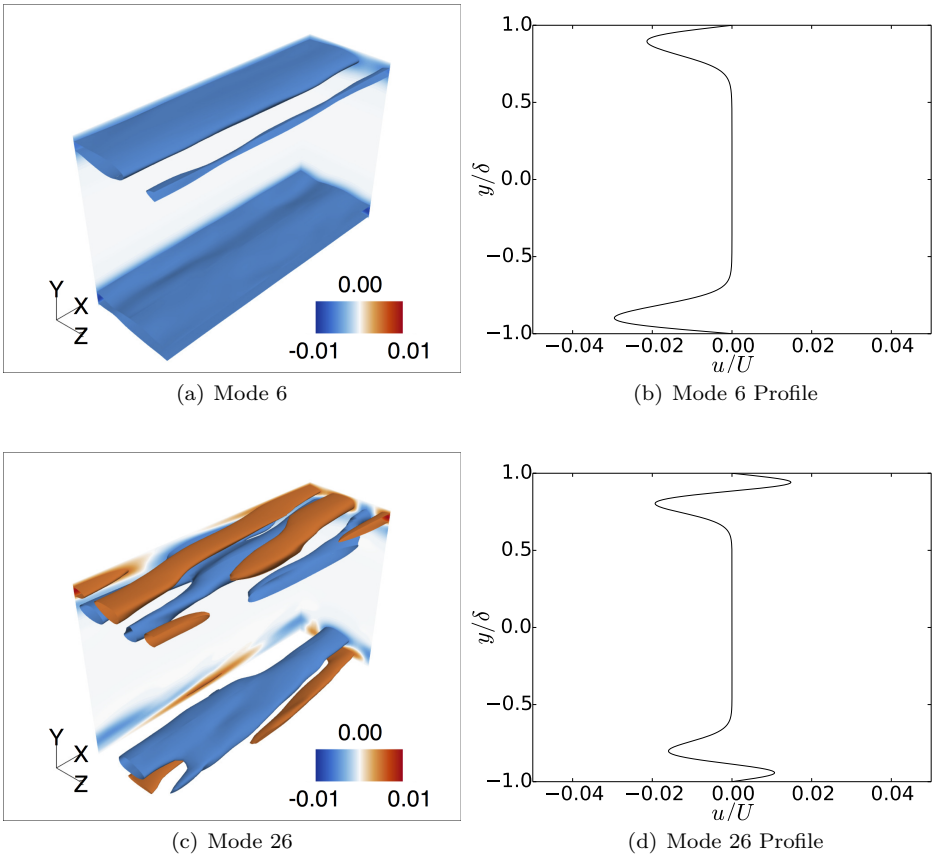

(a) Mode 6

(b) Mode 6 Profile

(c) Mode 26

(d) Mode 26 Profile

FIG. 10: Contours, isosurfaces, and spatially averaged profiles of axial velocity for the two most energetic POD modes in the optimal solution to Eq. (10). Isosurfaces are defined at $u \pm 0.01$.

Therefore, although the optimal solution $\boldsymbol{u}_0^*$ is turbulent, the absence of axial velocity streaks and quasi-streamwise vortices make it a precursor for a flow laminarization. By tracking how close a given state is to $\boldsymbol{u}_0^*$, we can determine if a laminarization event is likely to occur or not.

Although we can compute the precursor for the relatively low Reynolds number flows considered in this paper, the adjoint growth issue encountered for $\tau = 210t_e$ suggests that this approach will not scale well with Reynolds number. The adjoint grows exponentially in time at a rate roughly equal to the largest Lyapunov exponent of the flow [41]. The maximum Lyapunov exponent grows in turn as the Reynolds number increases [34]. As a result, computing the optimal solution at higher Reynolds numbers by a straightforward adjoint optimization may face numerical instability issues. Approaches like least squares shadowing have been shown to eliminate exponential growth of the adjoint for time-averaged objective functions [42], but to the authors' knowledge no such approach exists for transient objective functions like that in our optimization problem (6).

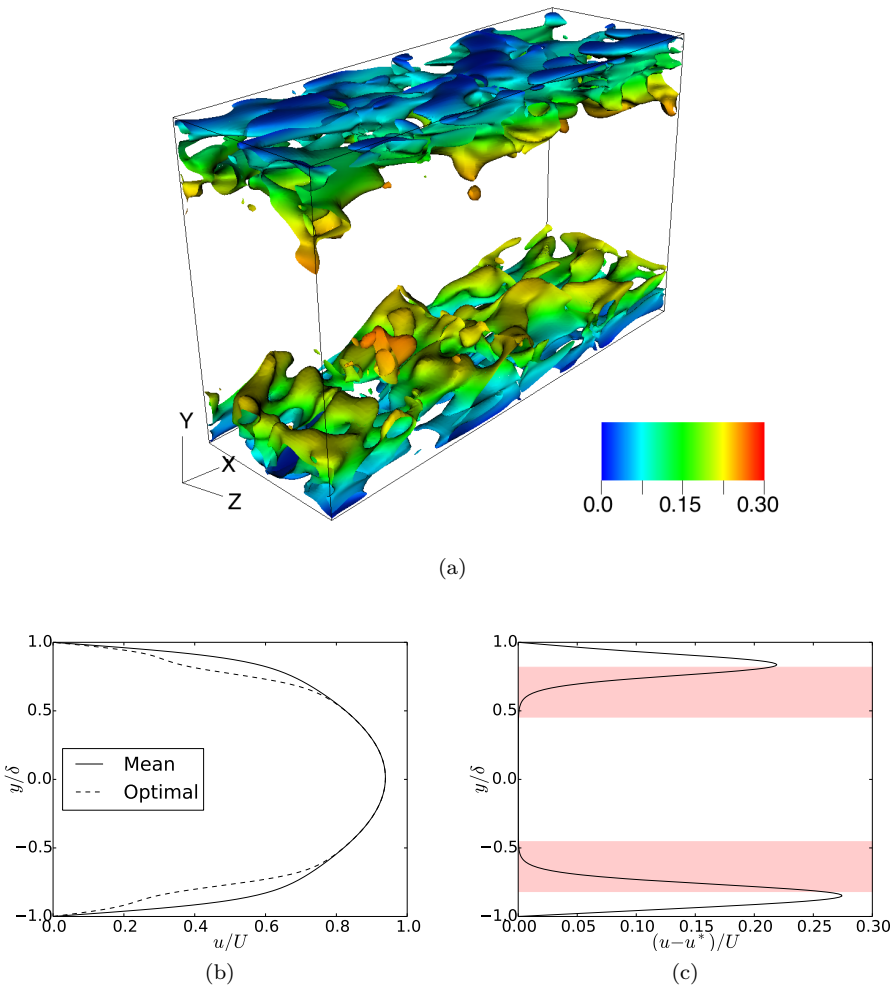

FIG. 11: Optimal solution $\boldsymbol{u}_0^*$ to equation (10). (a) Q criterion isosurface for $Q = 0.0005$, colored by the streamwise velocity (b) Spatially averaged streamwise velocity profile with the mean axial velocity profile. (c) Spatially averaged streamwise velocity profile difference. Red shaded boxes indicate regions from $y^+ = 20$ to $y^+ = 60$ units away from the wall.

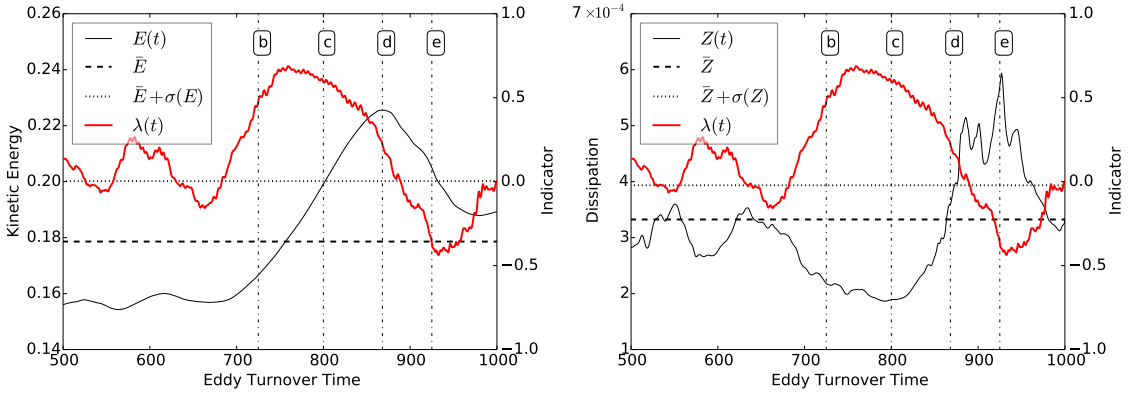

(a) (b)

FIG. 12: Time evolution of the indicator $\lambda(t)$ with $E(t)$ and $Z(t)$ over the same time horizon as shown in Fig. 2. The horizontal lines indicate the mean ($\bar{X}$) and the mean plus one standard deviation ($\bar{X}+\sigma(X)$) of $E(t)$ and $Z(t)$. The vertical lines indicate the times that snapshots in Fig. 3 correspond to. The first and last snapshot correspond to the start and end of the time horizon shown above.

IV. PREDICTING EXTREME EVENTS

Figure 12 shows a close-up of the evolution of energy E and dissipation Z together with the indicator

$$\lambda = \frac{\langle \boldsymbol{u} - \overline{\boldsymbol{u}}, \boldsymbol{u}_0^* - \overline{\boldsymbol{u}} \rangle}{\|\boldsymbol{u} - \overline{\boldsymbol{u}}\|_2 \|\boldsymbol{u}_0^* - \overline{\boldsymbol{u}}\|_2}, \tag{13}$$

at $Re = 2200$. Large values of energy and dissipation are proceeded with relatively large values of the indicator. This behavior turns out to be generic and not specific to this time window. As a result, one can use the indicator λ to predict the upcoming extreme events in the channel flow. In order to quantify these predictions, we first review some statistical tools in Section IV A. Subsequently, in Section IV B, we apply these tools to longterm simulations of the channel flow and report the results.

A. Statistical preliminaries

In this section, we show that the trigger state obtained previously can be used for the prediction of the extreme events in the channel flow. In order to make quantitative statements, we use joint and conditional statistics between the trigger mode and the energetic observables of the turbulent flow, namely kinetic energy and energy dissipation rate.

For a given random variable X_t, we would like to find an indicator Y_t (another random variable) whose values signal an upcoming extreme event of X_t. We identify extreme events of X_t as any instant where $X_t > x_e$ for a prescribed extreme value threshold x_e. First we define the maximum

value of the random variable X_t over a future time interval $[t+t_0, t+t_0+\Delta t]$ for some $t_0, \Delta t \geq 0$,

$$\tilde{X}_t(t_0, \Delta t) = \max_{s \in [t+t_0, t+t_0+\Delta t]} X_s \tag{14}$$

The maximum $\tilde{X}_t(t_0, \Delta t)$ is a new random variable which depends on the parameters t_0 and Δt. At any time t, $\tilde{X}_t(t_0, \Delta t)$ measures the maximum value that X_t will take over the future time interval $[t+t_0, t+t_0+\Delta t]$. For notational simplicity, we omit the parameters t_0 and Δt and simply write $\tilde{X}_t$.

The joint probability distribution of the pair $(\tilde{X}_t, Y_t)$ is defined by

$$\begin{aligned} F_{\tilde{X}_t, Y_t}(x, y) &= \mathbb{P}(\tilde{X}_t \leq x, Y_t \leq y) \\ &= \int_{-\infty}^{x} \int_{-\infty}^{y} p_{\tilde{X}_t, Y_t}(x, y) \mathrm{d}x \mathrm{d}y, \end{aligned} \tag{15}$$

where $p_{\tilde{X}_t, Y_t}$ is the probability density associated with the probability distribution $F_{\tilde{X}_t, Y_t}$. Roughly speaking, the quantity $p_{\tilde{X}_t, Y_t}(x, y)\mathrm{d}x\mathrm{d}y$ measures the probability that at time t we observe $x < \tilde{X}_t < x + \mathrm{d}x$ and $y < Y_t < y + \mathrm{d}y$.

The conditional probability of $\tilde{X}_t = x$ given that $Y_t = y$ is defined through the Bayes' formula

$$p_{\tilde{X}_t | Y_t} = \frac{p_{\tilde{X}_t, Y_t}}{p_{Y_t}}, \tag{16}$$

where p_{Y_t} is the probability density associated with the random variable Y_t. We use the conditional PDF $p_{\tilde{X}_t | Y_t}$ to quantify the extent to which the behavior of Y_t is indicative of the extreme events of X_t over the future time interval $[t+t_0, t+t_0+\Delta t]$. More precisely, given an extreme event threshold x_e, we define the probability of upcoming extreme events by

$$P_{ee}(y) = \int_{x_e}^{\infty} p_{\tilde{X}_t | Y_t}(x, y) \mathrm{d}x. \tag{17}$$

This quantity measures the probability of an extreme event over the future time interval $[t+t_0, t+t_0+\Delta t]$ given the current value of the indicator $Y_t = y$.

For a reliable indicator, P_{ee} should be monotonic so that the probability of upcoming extreme events increases with y. More precisely, P_{ee} should be nearly zero for small values of y and increase monotonically towards 1 as y increases. We predict an upcoming extreme only if $P_{ee} > 0.5$. This defines an extreme event threshold y_e for the indicator Y_t where $P_{ee}(y_e) = 0.5$. If $Y_t > y_e$ an upcoming extreme event is predicted and conversely if $Y_t < y_e$ it is predicted that no extreme events will occur over the future time interval $[t+t_0, t+t_0+\Delta t]$.

This classification leads to four possible prediction outcomes in terms of the indicator value Y_t and the future observable values $\tilde{X}_t$:

$$\begin{aligned} \text{Correct Rejection (CR):} \quad & \tilde{X}_t < x_e \quad \text{given} \quad Y_t < y_e, \\ \text{Correct Prediction (CP):} \quad & \tilde{X}_t > x_e \quad \text{given} \quad Y_t > y_e, \\ \text{False Negatives (FN):} \quad & \tilde{X}_t > x_e \quad \text{given} \quad Y_t < y_e, \\ \text{False Positive (FP):} \quad & \tilde{X}_t < x_e \quad \text{given} \quad Y_t > y_e. \end{aligned} \tag{18}$$

Therefore, the skill of an indicator for predicting upcoming extreme events can be quantifies as

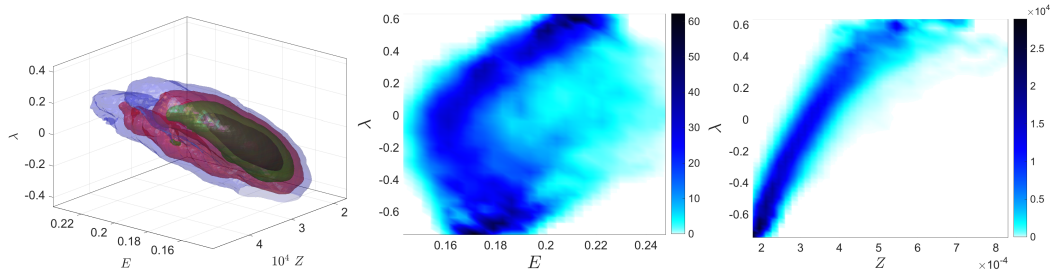

FIG. 13: Probability densities at $Re = 2200$. (a) Joint PDF of the kinetic energy E, energy dissipation Z and the indicator λ. (b) Conditional PDF $p_{E|\lambda}$. (c) Conditional PDF $p_{Z|\lambda}$.

follows

$$\text{Rate of successful predictions} = \frac{\text{CP}}{\text{CP} + \text{FN}} = \frac{\int_{x_e}^{\infty}\int_{y_e}^{\infty} p_{\tilde{X}_t|Y_t}(x,y)\mathrm{d}y\mathrm{d}x}{\int_{x_e}^{\infty}\int_{-\infty}^{\infty} p_{\tilde{X}_t|Y_t}(x,y)\mathrm{d}y\mathrm{d}x} \tag{19a}$$

$$\text{Rate of successful rejections} = \frac{\text{CR}}{\text{CR} + \text{FP}} = \frac{\int_{-\infty}^{x_e}\int_{-\infty}^{y_e} p_{\tilde{X}_t|Y_t}(x,y)\mathrm{d}y\mathrm{d}x}{\int_{-\infty}^{x_e}\int_{-\infty}^{\infty} p_{\tilde{X}_t|Y_t}(x,y)\mathrm{d}y\mathrm{d}x} \tag{19b}$$

A skillful indicator is one that returns relatively small percentage of false negatives (respectively, false positives) compared to the number of correct predictions (respectively, correct rejections). In the following, we use the statistical quantities introduced above to quantify the predictive skill of the indicator (13).

B. Prediction results

We first present the joint and conditional statistics for the energy E, dissipation rate Z and the indicator λ. In this first step, we do not include any time shifts, thus setting $t_0 = \Delta t = 0$ so that $\tilde{X}_t = X_t$ in equation (14). Figure 13 shows the joint and conditional PDFs of the indicator versus energy E and the energy dissipation Z at $Re = 2200$. This figure is generated from an ensemble of longterm simulations with data recorded every one eddy turnover time collecting a total of $106,063$ data points.

The shape of the conditional PDFs $p_{E|\lambda}$ and $p_{Z|\lambda}$ shows that the extreme values of the indicator λ correlate strongly with relatively large energy and large dissipation episodes (see Fig. 13(a,b)). We also note that that the correlation is much stronger for dissipation and that λ tends to increase monotonically with the dissipation Z.

The next step is to introduce a time lag in order to investigate whether the large indicator values precede the extreme episodes of energy and dissipation. This is clearly the case in figure 12 where

TABLE I: The prediction skill of the indicator λ at two Reynolds numbers. The rate of successful rejections (RSR) and the rate of successful predictions (RSP) are reported for the energy dissipation rate Z. The parameters t_0 and Δt denote the prediction time parameters defined in (14).

Re	t_0/t_e	$\Delta t/t_e$	RSP	RSR
2200	1	10	86.9%	94.7%
	2	10	86.7%	94.3%
	3	10	86.4%	93.8%
3000	1	5	79.4%	91.7%
	2	5	75.4%	92.6%
	3	5	74.9%	92.2%

the peak of the indicator precedes the extreme values of energy (and energy dissipation) by about 50 to 100 eddy turnover times. Below we show that this is generally the case during the longterm simulations. We point out, however, that figure 12 depicts an unusual extreme event in that the prediction time t_0 is very long. On average the prediction times are much shorter (on the order of a few eddy turnover times).

Figure 14 shows the conditional PDFs $p_{\tilde{E}|\lambda}$ and $p_{\tilde{Z}|\lambda}$ where the future maxima $\tilde{E}$ and $\tilde{Z}$ are computed with $t_0 = t_e$ and $\Delta t = 10t_e$ (see equation (14)). The extreme value threshold E_e (respectively, Z_e) are set as the mean of energy (respectively, dissipation) plus one standard deviation. Figure 14 also shows the corresponding P_{ee} computed from equation (17). The extreme event threshold according to the indicator λ is the point at which $P_{ee}(\lambda_e) = 0.5$.

As the prediction time t_0 increases, we expect the prediction skill of the indicator to deteriorate. This is shown in figure 15 where the conditional PDF $p_{\tilde{Z}|\lambda}$ are shown for increasing prediction times t_0. For prediction times as large as $t_0 = 10t_e$ the prediction skill of the indicator is still reasonably satisfactory. However, as the prediction time increases to close $t_0 = 25t_e$ the predictor returns significant amount of false positives and false negatives, thus losing its predictive value. The rates of successful predictions and successful rejections, defined in equation (19), are reported in Table I for a few prediction time horizons.

Similar results are observed at higher Reynolds numbers. Figure 16 shows the joint and conditional PDFs of the indicator, energy and dissipation at $Re = 3000$. These PDFs resemble those of figure 13 for the lower Reynold number $Re = 2200$. This demonstrates clearly the robustness of the derived indicator. Table I also contains the rates of success in predicting extreme (and non-extreme) events at $Re = 3000$. We point out that the channel flow at some intermediate Reynolds numbers between $Re = 2200$ and $Re = 3000$ did not exhibit extreme events in the time horizons we simulated.

Finally, we recall that the predictability time of chaotic systems is inversely proportional to their leading Lyapunov exponent [1] because of the exponential growth of uncertainties (This holds for both extreme and non-extreme events). Therefore, the prediction of extreme events is fundamentally limited by the predictability time horizon set by the leading Lyapunov exponent. Since the Lyapunov exponent increases with the Reynolds number, we expect the prediction time t_0 to decrease at higher Reynolds flows.

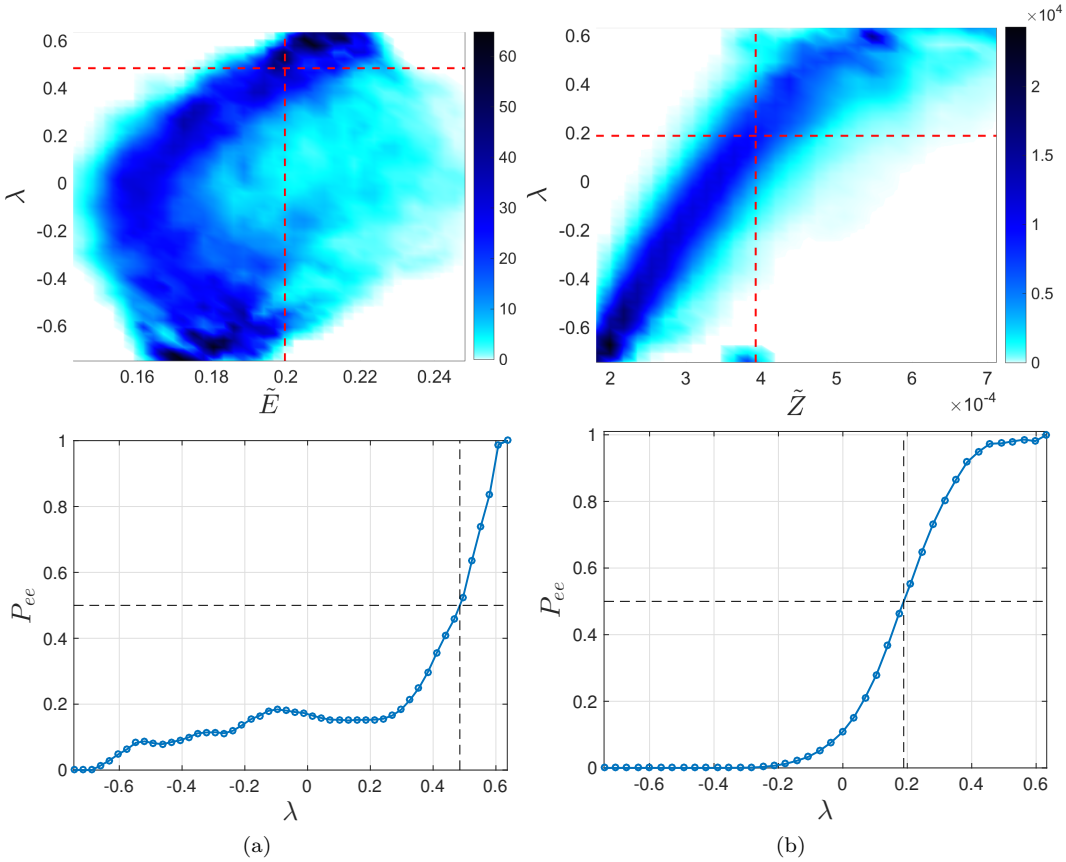

FIG. 14: Predictive conditional probability densities. (a) Top row: Conditional PDF $p_{\tilde{E}|\lambda}$ computed with $t_0 = t_e$ and $\Delta t = 10t_e$ where t_e denotes the eddy turnover time. The vertical dashed line marks the threshold E_e of extreme events that is prescribed as the mean of E plus one standard deviation. The horizontal dashed line marks the extreme event threshold λ_e according to the indicator λ. Bottom row: The probability of upcoming extreme events P_{ee}. The horizontal dashed line marks $P_{ee} = 0.5$ and the vertical dashed line marks the extreme event threshold λ_e so that $P_{ee}(\lambda_e) = 0.5$. (b) Same as panel (a) but the figure correspond to the energy dissipation Z versus the indicator λ.

V. CONCLUSIONS

We have demonstrated an original approach for the derivation of precursors of extreme events in a challenging problem involving a turbulent channel flow. The extreme events in this case have the form of random near-laminarization episodes that lead to bursts of the kinetic energy and the energy dissipation rate. We formulate a constrained optimization problem that searches for initial states with the most intense growth of kinetic energy, within a constrained set in the core of the underlying turbulent attractor. By searching over a high probability set, we achieve a numerically tractable optimization problem, while at the same time we exclude exotic states that may correspond to

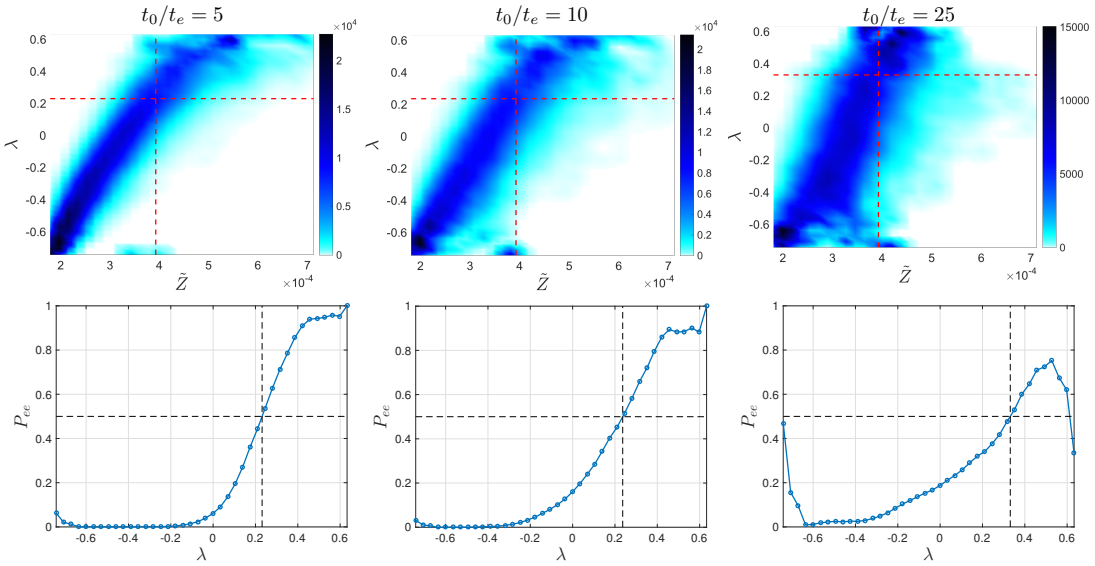

FIG. 15: Prediction quality for varying prediction times t_0. In all plots, the length of the future maximum time window in Eq. (14) is $\Delta t = 10$. First row shows the conditional PDF $p_{\tilde{Z}|\lambda}$ and the second row shows the corresponding probability of future extreme events defined in Eq. (17).

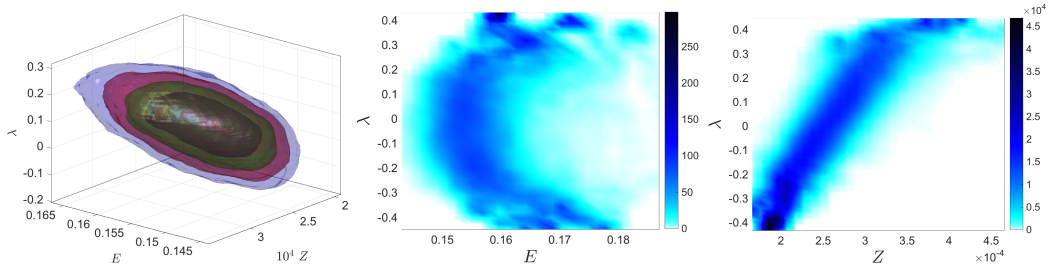

(a) (b) (c)

FIG. 16: Probability densities at $Re = 3000$. (a) Joint PDF of the kinetic energy E, energy dissipation Z and the indicator λ. (b) Conditional PDF of $Y_t =$ Indicator and $X_t =$ Energy. (c) Conditional PDF of $Y_t =$ Indicator and $X_t =$ Energy Dissipation.

intense growth of energy but have very low probability to occur if we are close to the attractor.

The derived precursor is demonstrated to successfully capture extreme dissipation episodes several eddy turnover times before the event. We have discussed its physical relevance and have demonstrated its robustness as the Reynolds number of the flow changes. Because the developed scheme utilizes the full nonlinear equations and not linearized approximations, it has the potential to be extended to more complex flows. However, one should exercise caution in using adjoint-based optimization at higher Reynolds numbers. As we mentioned in section III D, the straightforward backward integration of the adjoint equation at high Reynolds numbers is often unstable and therefore alternative optimization

methods should be considered.

Nonetheless, the success of the presented approach to an intermittently turbulent channel flow implies the potential of the method for studying transitional flows, such as bypass transition of boundary layers. Our future endeavors include the utilization of these precursors for the control and suppression of extreme events in these systems.

Acknowledgments

TPS and MF have been supported through the ARO MURI W911NF-17-1-0306 and the ONR grant N00014-15-1-2381. PJB was supported by an appointment to the NASA Postdoctoral Program at the NASA Ames Research Center, administered by Universities Space Research Association under contract with NASA. Specifically, the research efforts of PJB were sponsored by NASA's Transformational Tools and Technologies (TTT) Project of the Transformative Aeronautics Concepts Program under the Aeronautics Research Mission Directorate. Resources supporting this work were provided by the NASA High-End Computing (HEC) Program through the NASA Advanced Supercomputing (NAS) Division at Ames Research Center. We are also grateful to the anonymous referees for their comments which improved the presentation of this paper.

[1] K. T. Alligood, T. D. Sauer, and J. A. Yorke. *Chaos: An Introduction to Dynamical Systems*. Springer, 1996.

[2] H. Babaee, M. Farazmand, G. Haller, and T. P. Sapsis. Reduced-order description of transient instabilities and computation of finite-time Lyapunov exponents. *Chaos*, 27(6):063103, 2017.

[3] P. J. Blonigan. Adjoint sensitivity analysis of chaotic dynamical systems with non-intrusive least squares shadowing. *Journal of Computational Physics*, 348:803–826, 2017.

[4] H. A. Carlson and J. L. Lumley. Active control in the turbulent wall layer of a minimal flow unit. *Journal of Fluid Mechanics*, 329:341–371, 1996.

[5] M. A. Ceze, L. T. Diosady, and S. M. Murman. Development of a high-order space-time matrix-free adjoint solver. AIAA 2016-0833, January 2016.

[6] K. K. Chen, J. H. Tu, and C. W. Rowley. Variants of dynamic mode decomposition: boundary condition, Koopman, and Fourier analyses. *Journal of Nonlinear Science*, 22(6):887–915, 2012.

[7] D. Chung, L. Chan, M. MacDonald, N. Hutchins, and A. Ooi. A fast direct numerical simulation method for characterising hydraulic roughness. *Journal of Fluid Mechanics*, 773:418–431, 2015.

[8] C. Carton de Wiart, L. T. Diosady, A. Garai, N. K. Burgess, P. J. Blonigan, D. Ekelschot, and S. M. Murman. Design of a modular monolithic implicit solver for multi-physics applications. In *AIAA Aerospace Sciences Meeting, AIAA SciTech Forum*, number 2018-1400. AIAA, 2018.

[9] C. Carton de Wiart and S. M. Murman. Assessment of wall-modeled les strategies within a discontinuous-galerkin spectral-element framework corentin carton de wiart, nasa ames research center. In *55th AIAA Aerospace Sciences Meeting and Exhibit*, 2017.

[10] G. Dematteis, T. Grafke, and E. Vanden-Eijnden. Rogue Waves and Large Deviations in Deep Sea. *Proceedings of the National Academy of Sciences*, (10.1073/pnas.1710670115), 2018.

[11] L. T. Diosady and S. M. Murman. Design of a Variational Multiscale Method for Turbulent Compressible Flows. In *21th AIAA Computaional Fluid Dynamics Conference*, 2013.

[12] L. T. Diosady and S. M. Murman. Dns of flows over periodic hills using a discontinuous galerkin spectral element method. AIAA paper, 2014. accepted for publication.

[13] L. T. Diosady and S. M. Murman. Higher-order methods for compressible turbulent flows using entropy variables. In *53rd AIAA Aerospace Sciences Meeting and Exhibit*, 2015.

[14] M. Farano, S. Cherubini, J.-C. Robinet, and P. De Palma. Optimal bursts in turbulent channel flow. *J. Fluid Mech.*, 817:35–60, 2017.
[15] M. Farazmand. An adjoint-based approach for finding invariant solutions of Navier-Stokes equations. *J. Fluid Mech.*, 795:278–312, 2016.
[16] M. Farazmand and T. Sapsis. Dynamical indicators for the prediction of bursting phenomena in high-dimensional systems. *Physical Review E*, 032212:1–31, 2016.
[17] M. Farazmand and T. P. Sapsis. A variational approach to probing extreme events in turbulent dynamical systems. *Science Advances*, 3(9):e1701533, 2017.
[18] M. Farazmand and T. P. Sapsis. Extreme Events: Mechanisms and Prediction. *ASME Applied Mechanics Review*, 2019. In press.
[19] O. Florez and J. Jimenez. Hierarchy of minimal flow units in the logarithmic layer. *Physics of Fluids*, 22(7):071704, 2010.
[20] A. Garai, L. T. Diosady, S. M. Murman, and N. K. Madavan. High-pressure turbine cascade using a spectral-element discontinuous-Galerkin method. In *Proceedings of ASME Turbo Expo 2017, no. GT2017-64697*, Charlotte, USA, June 2017.
[21] P. Holmes, J. Lumley, and G. Berkooz. *Turbulence, Coherent Structures, Dynamical Systems and Symmetry*. Cambridge University Press, 1996.
[22] J. Jimenez. Cascades in wall-bounded turbulence. *Annual Review of Fluid Mechanics*, 44:27–45, 2012.
[23] J. Jiménez. Coherent structures in wall-bounded turbulence. *J. Fluid Mech.*, 842:P1, 2018.
[24] J. Jimenez and P. Moin. The minimal flow unit in near-wall turbulence. *Journal of Fluid Mechanics*, 225:213–240, 1991.
[25] J. Jimenez and A. Pinelli. The autonomous cycle of near-wall turbulence. *Journal of Fluid Mechanics*, 389:335–359, 1999.
[26] J. Jimenez and M. P. Simens. Low-dimensional dynamics of a turbulent wall flow. *Journal of Fluid Mechanics*, 435:81–91, 2001.
[27] E. Jones, T. Oliphant, P. Peterson, et al. SciPy: Open source scientific tools for Python, 2001–. [Online; accessed 7/11/18].
[28] J. Kim, P. Moin, and R. Moser. Turbulence statistics in fully developed channel flow at low Reynolds number. *Journal of Fluid Mechanics*, 177:133–166, 1986.
[29] J. N. Kutz, Xi. Fu, and S. L. Brunton. Multi-Resolution Dynamic Mode Decomposition. 15(2):713–735, 2015.
[30] M. MacDonald, D. Chung, N. Hutchins, L. Chan, A. Ooi, and R. Garcia-Mayoral. The minimal-span channel for rough-wall turbulent flows. *Journal of Fluid Mechanics*, 816:5–42, 2017.
[31] I. Mezić. Analysis of fluid flows via spectral properties of the Koopman operator. *Annual Review of Fluid Mechanics*, 45:357–378, 2013.
[32] M. A. Mohamad, W. Cousins, and T. P. Sapsis. A probabilistic decomposition-synthesis method for the quantification of rare events due to internal instabilities. *Journal of Computational Physics*, 322:288–308, 2016.
[33] M. A. Mohamad and T. P. Sapsis. Probabilistic description of extreme events in intermittently unstable dynamical systems excited by correlated stochastic processes. *SIAM/ASA Journal on Uncertainty Quantification*, 3(1):709–736, 2015.
[34] P. Mohan, N. Fitzsimmons, and R. D. Moser. Scaling of Lyapunov exponents in homogeneous isotropic turbulence. *Phys. Rev. Fluids*, 2:114606, Nov 2017.
[35] C. C. T. Pringle and R. R. Kerswell. Using nonlinear transient growth to construct the minimal seed for shear flow turbulence. *Phys. Rev. Lett.*, 105(15):154502, 2010.
[36] C. W. Rowley, I. Mezić, S. Bagheri, P. Schlatter, and D. S. Henningson. Spectral analysis of nonlinear flows. *J. Fluid Mech.*, 641:115–127, 2009.
[37] T. P. Sapsis. New perspectives for the prediction and statistical quantification of extreme events in high-dimensional dynamical systems. *Phil. Trans. R. Soc. Lond. A*, 376:20170133, 2018.
[38] T. P. Sapsis and A. J. Majda. A statistically accurate modified quasilinear Gaussian closure for uncertainty quantification in turbulent dynamical systems. *Physica D*, 252:34–45, 2013.
[39] T. P. Sapsis and A. J. Majda. Statistically accurate low-order models for uncertainty quantification in turbulent dynamical systems. *Proceedings of the National Academy of Sciences of the United States of*

America, 110(34), 2013.

[40] P. J. Schmid. Dynamic mode decomposition of numerical and experimental data. *J. Fluid Mech.*, 656:5–28, 2010.

[41] Q. Wang and J. Gao. The drag-adjoint field of a circular cylinder wake at Reynolds numbers 20, 100 and 500. *Journal of Fluid Mechanics*, 730:145–161, 2013.

[42] Q. Wang, R. Hui, and P. Blonigan. Least squares shadowing sensitivity analysis of chaotic limit cycle oscillations. *Journal of Computational Physics*, 267:210–224, June 2014.

[43] M. O. Williams, I. G. Kevrekidis, and C. W. Rowley. A data–driven approximation of the Koopman operator: Extending dynamic mode decomposition. *Journal of Nonlinear Science*, 25(6):1307–1346, 2015.